npj computational materials

www.nature.com/npjcompumats

ARTICLE OPEN

Check for updates

Thermo-electro-mechanical microstructural interdependences in conductive thermoplastics

Javier Crespo-Miguel[1], Sergio Lucarini[2], Angel Arias[1] and Daniel Garcia-Gonzalez[1]✉

Additive manufacturing has enabled the design of thermoplastic components that provide structural support, electrical conductivity and heat generation modulated by mechanical deformation. The mechanisms and interplays that govern the material response at the microstructural level remain, however, elusive. Here, we develop an experimental method to characterise conductive filaments from a combined mechanical, electrical and thermal perspective. This approach is used to unravel exciting material interplays of conductive polylactic acid. To overcome experimental limitations that prevent a complete microstructural analysis of the problem, we develop a full-field homogenisation framework and implement it for finite elements. The framework accounts for viscoplasticity, electrical and thermal conduction, convection and heat generation via Joule effect, as well as for the interdependences between them. After experimental validation, the framework is applied to virtually optimise fabrication requirements to obtain desired properties in final products, i.e., stiffer products, filaments with higher conductivities or with better sensing capabilities.

npj Computational Materials (2023)9:134 ; https://doi.org/10.1038/s41524-023-01091-8

INTRODUCTION

Due to their deformation-sensitive properties, conductive polymeric composites have great potential in sensors for soft-robotics[1,2], flexible electronics[3,4] or electromagnetic interference shielding[5]. The addition of conductive particles, such as metallic powders[6–9] or carbon-based particles (e.g., carbon nanotubes[10–13], graphene[14–17], Carbon Black[18,19] or carbon nanofibers[20]), to polymeric matrices alters their natural insulating properties, allowing the flow of electric current. As a result, these materials experience temperature changes due to the Joule effect, which enables them to be used as local heat generators[21]. These filled conductive polymers can be formulated in various forms, depending on the polymeric matrix used (i.e., thermoplastic[10,22–26], elastomer[3,27], or hydrogel[28–31]) as well as the conductive filler employed. Elastomeric and hydrogel matrices are great candidates for low stiffness applications such as soft-robots[32–34], flexible electronics[31,35,36] or biomedical devices[29,37,38], whereas photocurable polymers and thermoplastics better fulfil the requirement for higher stiffness applications. The behaviour of conductive thermoplastics is extremely complex due to the numerous intrinsic multifunctional couplings such as thermal, electrical and mechanical interdependencies. This complexity is further compounded when filament extrusion (FFF) is employed in the manufacturing process, due to filament bonding and the resulting anisotropic porosity[39,40]. From the material perspective, one of the main limitations of thermoplastics is the significant dependence of their mechanical properties on temperature[21,41], which is a critical concern since the flow of electric current through the composite generates in turn heat within the solid. Thus, the addition of conductive particles to a thermoplastic not only changes the mechanical behaviour of the solid due to particle-matrix interactions but also due to electro-thermal effects[10,21,42]. Additionally, mechanical deformation of the composite alters the distribution of the particles, resulting in changes in the electrical behaviour due to modifications in the conductive pathways[1,3,9].

The printing parameters used during the FFF process strongly influence the mesostructural features of the printed component, which, in turn, affect the overall material behaviour[21,42]. However, it is still unclear whether these changes in material response are uniquely explained by the final mesostructure of the printed component, or if there are also changes at the material level (i.e., deposited filament). The thermo-electro-mechanical response of a conductive device at the macroscopic level is dependent on the geometry and boundary conditions, including zones that exhibit stress or current concentrations, or zones with high/low exposure to convection[25]. At the mesoscopic level, micro-voids are created during the FFF process due to the imperfect adhesion between extruded filaments, which have a preferred direction defined by the printing orientation. Thus, the material response at this level is determined by the relation between loading direction (both thermal, electrical and mechanical) and printing orientation[21]. From a microscopic viewpoint, the material behaviour is governed by the nature and distribution of the composite phases (e.g., polymeric matrix and conductive particles) as well as the formation and distribution of micro-voids[7,12,16]. Therefore, to understand the response of 3D printed conductive devices, the thermo-electro-mechanical response of these composites must be studied at a microscopic level. To this end, the analysis of the conductive thermoplastic filament would isolate the material behaviour by discarding structural effects.

The experimental study of conductive FFF filaments has been addressed numerously, tackling its response from different points of view. For instance, several research works manufactured PLA composites with the addition of carbon-based nanoparticles, performing electrochemical analysis[43–45]. Conductivity analysis was carried out for filaments with a variety of polymeric matrices and conductive fillers, mostly applying a percolation approach[8,13,16,46]. Additionally, composites' conductivities or

[1]Department of Continuum Mechanics and Structural Analysis, Universidad Carlos III de Madrid, Avda. de la Universidad 30, 28911 Leganés, Madrid, Spain. [2]Department of Civil and Environmental Engineering, Imperial College of London, South Kensington Campus, London SW7 2AZ, UK. ✉email: danigarc@ing.uc3m.es

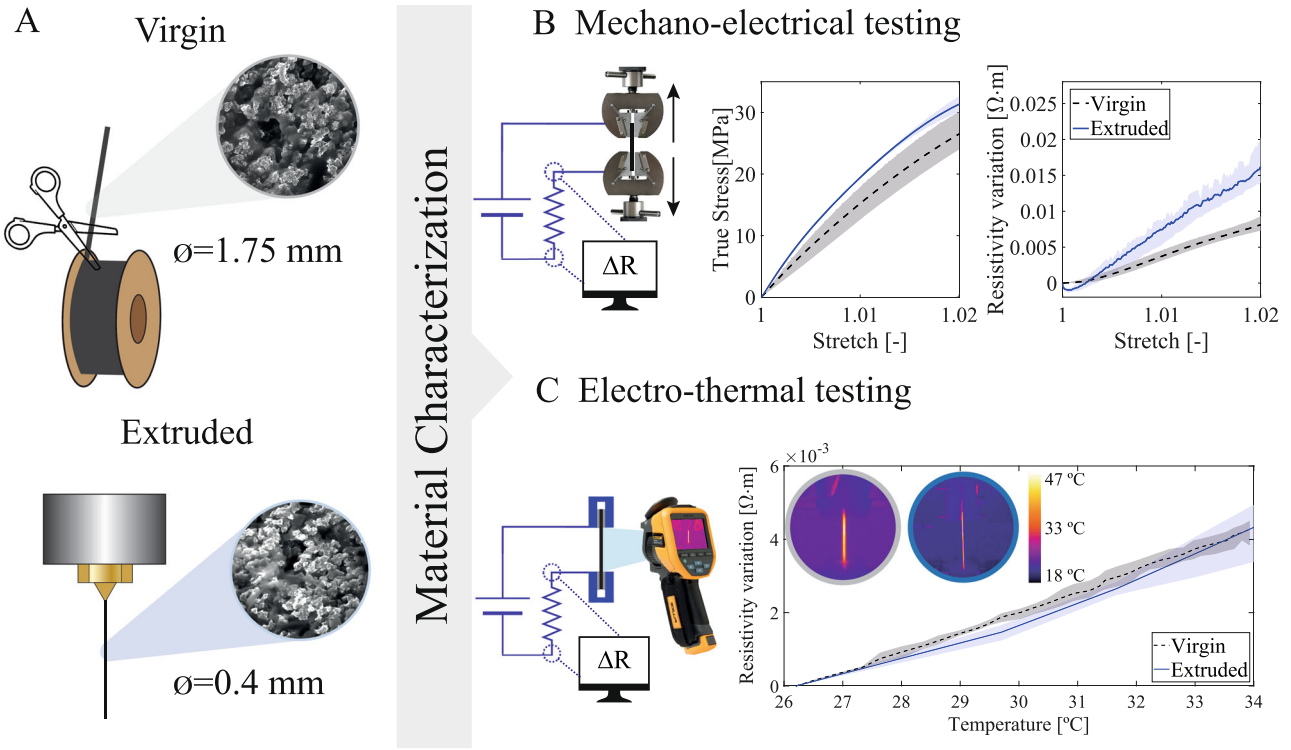

Fig. 1 Experimental comparison of the mechano-electrical and electro-thermal behaviour of spool-filaments (virgin) and extruded-filaments. A Scheme of sample preparation. The virgin samples were directly cut from the commercial spool (diameter of 1.75 mm). Extruded samples were cut after filament extrusion using a nozzle diameter of 0.4 mm. **B** Uniaxial tensile testing of virgin and extruded samples at strain rate of 0.00125 s^{-1}. During these tests, the electrical resistivity of the samples is measured over time. **C** Evaluation of Joule heating on virgin and extruded samples exposed to a constant DC field of 10 V for virgin samples and 44 V for extruded samples, to ensure equivalent Joule heating. Both temperature and resistivity were measured during the experiment. The variation of resistivity is plotted against temperature. Three samples were used for each test condition. The shaded areas represent the experimental deviation, while the solid/dashed lines represent the mean response.

thermal dilatation coefficients were analysed from a thermal point of view[15,16,22,46,47], and the tensile strength of conductive composites in filament form was also studied in[13,15]. Most research efforts have focused on the thermo-electro-mechanical response of printed samples, which adds strong structural effects due to the additive manufacturing (AM) process[11,48]. Nevertheless, to the best of the authors' knowledge, there is no work addressing the thermal, electrical and mechanical responses of conductive filaments in a coupled fashion, taking into account the different interplays that occur between those physics.

In this work, we aim at addressing the current literature gap regarding three main areas: (i) the analysis of single-filament conductive materials; (ii) the study of the fully coupled thermo-electro-mechanical response of conductive 3D printed polymers; and (iii) the computational modelling of the thermo-electro-mechanical behaviour of these materials based on their microstructure. To this end, we conducted a multi-physics experimental campaign on conductive filaments using a commercial filament spool based on a PLA matrix filled with Carbon Black conductive particles. The experiments tackled the multi-physical problem in two ways: (i) by studying the interdependencies between physics by pairs, isolating the one-to-one interplays; and (ii) by analysing the fully coupled response of the material through a test where thermal, electrical, and mechanical loadings were considered simultaneously, excluding (macro- and meso-) structural effects. Although these results provided valuable insights into the thermo-electro-mechanical response of conductive thermoplastics, it was insufficient to provide a complete understanding of the underlying microstructural mechanisms. To overcome this limitation, we proposed a full-field homogenisation framework that considers all the interplays observed in conductive thermoplastics. The computational framework presented here captures the macroscopic response observed in the experiments by considering periodic Representative Volume Elements (RVE) of the microstructure. The complete framework was finally proved as a valuable tool to guide the design of material composition depending on the final application.

RESULTS

Extrusion maintains multifunctional conductive response

To explore the potential effects of the filament extrusion process on its properties, we provide a characterisation analysis consisting of (i) mechano-electrical and (ii) electro-thermal tests, for both virgin and printed filaments. Note that we refer to coupling tests following the nomenclature *input physic-output physic*. The former evaluate stress and electrical resistivity changes when the filament is subjected to stretching. The latter evaluate temperature evolution within the sample when exposed to a constant electric potential over time, accounting for the change in temperature due to Joule heating, which also affects the electrical resistivity of the material. These results are presented in Fig. 1, facilitating the multifunctional comparison between virgin and printed filaments. The mechano-electrical results showed no significant changes in the mechanical response of the material at room temperature, with similar maximum stress (≈30 MPa) and Young's modulus (1.7–2.3 GPa) (Fig. 1B). However, the printed filaments showed a higher sensitivity in terms of electrical resistivity variation under stretching conditions. Note that the printed samples were extruded through a slim nozzle (0.4 mm),

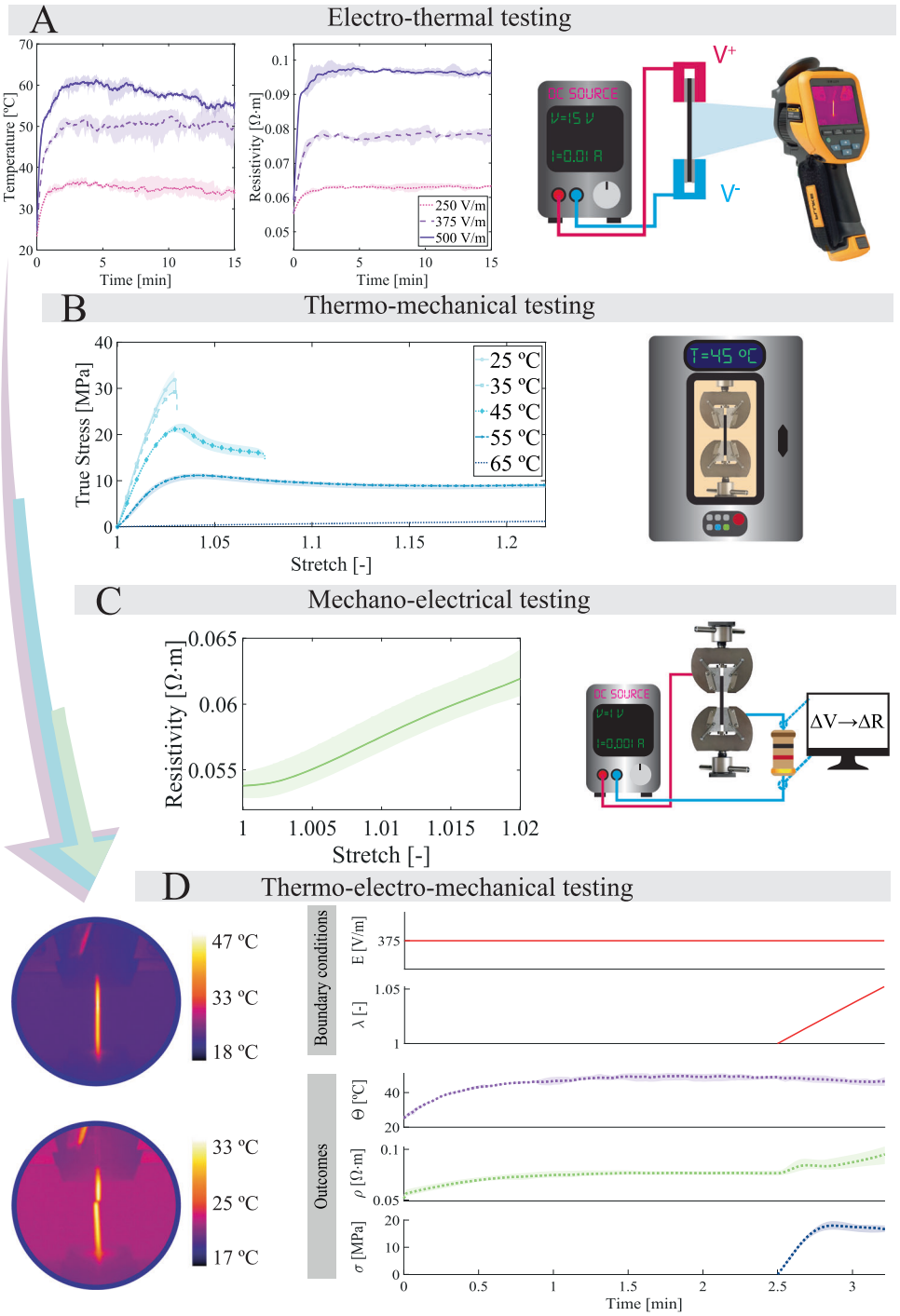

Fig. 2 Multifunctional characterisation of conductive PLA at filament level and multiphysics experimental framework. A Electro-thermal characterisation analysing Joule heating for three different electrical fields: 250 V m^{-1}; 375 V m^{-1}; and 500 V m^{-1}. Both temperature and electrical resistivity are represented versus time. **B** Thermo-mechanical characterisation under uniaxial tensile testing and controlled temperature conditions. Five different temperatures were considered: 25, 35, 45, 55 and 65 °C. **C** Mechano-electrical characterisation measuring the electrical resistivity of the material during uniaxial tensile conditions. **D** Fully coupled multi-physics testing. The complete experimental framework was used to control the temporal evolution of the mechanical (displacement control) and electrical fields. As outcomes, mechanical stress, sample temperature and electrical resistivity were measured over time. Two representative infrared images of the experiment are presented: at the beginning of the mechanical loading; and at mechanical failure. The shaded areas of the different graphs represent the experimental deviation. Three samples were used for each testing condition.

resulting in smaller diameters and higher variability over length. Nevertheless, both tendencies and magnitudes remain similar between virgin and extruded samples, allowing the extrapolation of their mechano-electrical behaviour. Regarding the electro-thermal results (Fig. 1C), they showed negligible differences in the relation between electrical resistivity and temperature, with a mean temperature coefficient of resistivity of 0.01 $°C^{-1}$. These results indicate that the extrusion process did not significantly affect the mechanical, electrical and thermal properties of the filament.

Filament-scale couplings for conductive 3D thermoplastics

The comprehensive characterisation of conductive composites faces important challenges to isolate mechanical, thermal and electrical responses. As shown in the results collected in Fig. 1, these responses are interdependent, creating a complex feedback loop. Therefore, the advance in the field requires new methodologies to allow a complete multi-physical analysis. Ideally, such an experimental framework would allow for controlling mechanical (displacement field), thermal (temperature) and electrical (electric potential) variables while enabling the measurement of the three problem outcomes (mechanical stresses, temperature fields and electrical resistivity). Here, we present an advanced testing framework that integrates a uniaxial testing device, a thermal chamber equipped with thermocouples, a thermal IR camera, and an electrical circuit to impose controlled DC fields on the sample (see Supplementary Methods for more details). In addition, the whole setup is adapted to the analysis of single-filament samples, allowing the characterisation at the material level, and preventing structural effects from the analysis due to the printing process.

For the sake of isolating the coupling that appears between the three physics of the problem, we conducted several two-physics multifunctional analyses on single-filament samples, i.e., electro-thermal, thermo-mechanical and electro-mechanical tests. The electro-thermal experiments were performed by imposing different DC fields (250, 375 and 500 V m^{-1}) on the samples and measuring the evolution of temperature over time due to Joule heating. Note that this increase in temperature causes a change in the electrical resistivity, leading to a bidirectional coupling between the electrical and thermal contributions. Overall, temperature and resistivity stabilise when the equilibrium between convection and Joule heating contributions is reached. These results are collected in Fig. 2A and show higher stabilisation temperatures and resistivities for higher DC fields, which is consistent with previous results at the structural level[21]. Regarding thermo-mechanical coupling, thermoplastic composites exhibit a clear dependence of their mechanical behaviour on temperature. We conducted uniaxial tensile experiments on filament samples exposed to five testing temperatures ranging from room temperature (25 °C) to 65 °C, exceeding glass transition temperature but still below the melting point. The results are presented in Fig. 2B and show a reduction in stiffness and maximum stress with temperature. Nevertheless, an increase in temperature also enhances the composite ductility from a brittle response in the range of 25 to 35 °C, to a ductile response above 45 °C. After surpassing the glass transition temperature, the material undergoes a completely plastic behaviour, exhibiting negligible stiffness compared with the remaining temperatures tested. Finally, we assessed the interdependence between mechanical and electrical behaviour. In this regard, the electric current flow is determined by the nature and spatial arrangement of the conductive particles within the composite. Therefore, under stretching conditions, these particles experience relative displacements that result in electrical resistivity alterations. This coupling is analysed by integrating an electrical circuit to the sample tested within the universal testing device. These results are presented in Fig. 2C, showing a marked change in resistivity due to uniaxial stretching following a linear trend, with a mean gauge factor of 5.5.

After the analysis of multifunctional couplings by pairs, we evaluated the capability of the proposed experimental testing framework to conduct fully coupled experiments in which temporal variations in mechanical, thermal, and electrical boundary conditions (BCs) are modulated, see Fig. 2D. Filament samples were placed in the universal testing machine under fixed null displacements while imposing a constant electric field of 375 V m^{-1}. After 2.5 min under these BCs, a stretching ramp was applied while keeping the electric field constant. Throughout the experiment, the temperature, electrical resistivity and mechanical stress were measured. The results showed an increase in temperature due to the Joule effect arising from the electrical BCs, which stabilised in 1 min. This increase also impacted the electrical resistivity, which increased until reaching a stabilised value. When stretching was applied, a marked increase in electrical resistivity was appreciated due to material deformation and the subsequent relative displacements between conductive particles at the microstructural level. In addition, although the experiment is performed at room temperature, the mechanical response of the filament showed a ductile response due to the temperature increase in the first stage of the experiment. Interestingly, a slight decrease in sample temperature was observed after stretching. This can be explained by the increase in electrical resistivity due to material deformation and the subsequent impact in Joule heating (see Supplementary Fig. 2 for a more detailed representation). These results reveal how couplings that, individually, are inherently unidirectional, e.g., mechano-electrical coupling, can act as bidirectional when considering the remaining variables.

Microstructural model explains conductive thermoplastics' behaviour

The previous experimental results have revealed the complex and interdependent multifunctional responses in conductive PLA. To gain a deeper understanding of these results from a microstructural perspective, complementary methods are required. Such an approach is crucial in uncovering the mechanisms that govern these multifunctional responses in conductive thermoplastic composites. Understanding the interactions between the particles and matrix from a microstructural perspective, such as microporosity and particle rearrangement due to mechanical deformation, is essential. However, the high contrast in material properties, i.e., mechanical stiffness and electrical conductivity, makes it difficult to intuitively analyze the thermo-electro-mechanical response.

To overcome experimental limitations and tackle this problematic, we developed a virtual testing framework based on in silico approaches. Our approach consists in a full-field homogenisation model that accounts for the fundamental aspects and mechanisms of the problem. From a microstructural view, we synthetically generated Representative Volume Elements (RVEs) of the microstructure considering the periodic arrangement of three material phases, i.e., PLA matrix, CB particles and micro-voids. From a mechanical viewpoint, we implemented specific constitutive models for each phase considering viscoplastic behaviour and temperature dependences. Regarding the thermal problem, apart from stiffness dependence on temperature, we introduced conduction, natural convection and Joule heating in the formulation. For the electrical physics, we accounted for the different conductivities of the material phases and their temperature dependence. The whole formulation was implemented in a finite element framework for finite deformations that takes displacements, electrical and temperature fields as independent variables. In addition, we imposed periodic boundary conditions in the RVEs and solved the coupled problems following an implicit integration algorithm that includes macroscopic and fluctuating fields. The modelling approach relies on the far-field conditions (macroscopic) of the virtual test, which determine the equilibrium outcomes of effective stress, current flow, and temperature. These far-field conditions serve as inputs for the computational model, allowing for the accurate prediction of the material's multifunctional response under various loading and environmental conditions (see Methods and Supplementary Material for details). Therefore, our modelling framework allows for linking the macroscopic responses with the microstructural interactions by applying boundary conditions equivalent to the experimental ones.

Our framework was validated by one-to-one comparison with experiments shown in Fig. 2 and the results obtained from the virtual tests are presented in Fig. 3. Following the same methodology as in the experimental study, we first analysed the coupled responses by pairs of physics. From an electro-thermal perspective, the model reproduces the effects of temperature increase by Joule effect on decreasing electrical conductivity, which in turn leads to a subsequent diminish of Joule heating. The stabilisation is reached when convection cooling and Joule heating are balanced. Note that, as for the experimental evidence, the required time to reach this stabilisation is independent of the electric field applied. Moreover, the mechanical dependence on temperature arises mainly from the polymeric matrix, while the CB particles are considered temperature independent, and the micro-voids do not provide any mechanical stiffness to the RVE at any temperature. Due to the large difference in stiffness between phases, the CB particles behave almost as a rigid solid in comparison with the PLA matrix. Thus, the particles provide an increase in stiffness to the overall composite, whereas the nonlinear mechanical response is mainly controlled by the PLA matrix. Regarding the micro-voids, their negligible stiffness contributes to lower stiffness and yield stress of the composite. From a mechano-electrical perspective, the model reproduces how the imposed stretch leads to a separation of the conductive particles, thereby modifying the electric field distribution within the solid and modulating the current density flow. This change in current density is translated into a modification of the macroscopic composite resistivity. Finally, we tested our computational framework under fully coupled thermo-electro-mechanical simulations. To this end, we numerically reproduced the experiment presented in Fig. 2D. These results are shown in Fig. 3D, where the experimentally observed bidirectional couplings are successfully captured.

Virtual framework to design conductive thermoplastics

The multifunctional properties of conductive thermoplastics are determined by geometrical factors at two levels: (i) the filaments bonding and the resulting mesostructural distribution of macro-voids, and (ii) the microstructural arrangement of the conductive particles and distribution of micro-voids. The first geometrical factors can be evaluated in a more straightforward manner by characterising samples printed under different conditions (e.g., different printing directions, layer height, etc.). However, the evaluation of the second factor is highly complex from a purely experimental approach and would require very long testing times. In this regard, the resistivity of the composite arises from the multiple potential factors concerning the distribution of conductive particles, which favour or hinder the formation of conductive paths, e.g.,: the aspect ratio[6,13,17], the particle dispersion[49,50] or the cluster formation[51], among others. The control of these factors along with the formation and distribution of micro-voids would allow for modulating the final resistivity of the material as well as the mechanical and electro-thermal responses. Although an experimental evaluation of all these factors and their interplays would be unapproachable, the proposed full-field model can explicitly account for them, allowing the virtual testing of the multifunctional response of the composite.

Using the proposed computational framework and taking the conductive PLA as baseline material, we performed a parametric sweep study of the effect of micro-void and particle volume ratios. Firstly, we subjected different RVEs to mechanical stretch while imposing a low and constant macroscopic electric field. Three main outcomes were collected: effective stiffness, pre-deformation effective conductivity and gauge factor. Secondly, we evaluated the thermo-electrical coupling of the composites by applying a constant macroscopic electric field until stabilisation and measuring the resulting stabilisation temperature due to Joule heating. The main results of this numerical analysis are presented in Fig. 4, illustrating the four main outcomes obtained from the parametric sweep study.

Regarding the mechanical properties of the material, the effective stiffness is modulated by both particle and micro-void volume ratios. As the particle content increases, the composite stiffness does accordingly, whereas an increase in the micro-void volume ratio causes a reduction in stiffness. However, the computational results demonstrate that the micro-void content is the primary factor modulating the mechanical properties of the composite. The increase in stiffness caused by the addition of particles is countered by the micro-voids when their content exceeds 15%, leading to a lower Young's modulus than the pure PLA matrix. This explains an a priori counterintuitive experimental observation in previous studies using conductive PLA[21,42]. From an electrical perspective, the conductive particle content is the main parameter affecting the conductivity of the composite. For a constant particle volume ratio, the content of micro-voids decreases the final composite conductivity, due to the lower probability of electron tunneling between particles separated by voids than those separated by PLA matrix[52,53]. In terms of electro-thermal response, the stabilisation temperature shows similar outcomes as from the conductivity analysis. This can be explained by the dependence of Joule heating on conductivity and the ease of the temperature to homogenise at a microscopic scale. Note that the temperature gradients within the RVEs, caused by the differences between phases' thermal conductivities, are negligible. Regarding the mechano-electrical sensing capabilities, the micro-void content appears to slightly increase the gauge factor when the conductive particles content allows for a sufficient electrical current. The increase in micro-voids causes higher local deformations between conductive particles, leading to a higher increase in local resistance and, therefore, a larger gauge factor. However, note that a higher gauge factor does not necessarily imply better sensing performance in real-world applications. In this regard, this information should be considered along with the apparent conductivity, seeking high gauge factors while ensuring suitable operational conductivity/resistivity values.

DISCUSSION

The multi-physical behaviour of conductive 3D printing filaments has been proven to be highly complex, showing several interplays between electrical, thermal and mechanical responses. Previous works showed structural anisotropy derived from 3D printing, that hinders an intuitive analysis of the material's behaviour[21,42]. To overcome the limitations of previous studies to date, we provide herein a novel multi-physics experimental campaign at the single-filament level, as well as a complete computational framework. The experimental work approaches the thermo-electro-mechanical problem by tackling the interplays between physics by pairs and ultimately conducting a fully coupled experiment. To complement the experimental observations and gain deeper insights, the proposed full-field model is used to better understand the microstructural mechanisms of the thermal, electrical, and mechanical processes occurring within a Representative Volume Element (RVE).

The experimental results exhibit how conductive PLA filaments maintain good mechanical properties after the addition of conductive particles to the polymeric matrix. In addition, we demonstrate, at a filament level, that this material can be used for heatable devices by applying low voltages (i.e., within the range of batteries power). Following these ideas, conductive PLA filaments could be used to manufacture heatable sockets for DIW printers, in cases where a small and controlled heating could improve the polymerization of DIW inks during printing[3]. Moreover, the gauge factor (strain sensing capabilities) of conductive PLA is comparable to that of materials used for traditional strain gauges. Thus, strain

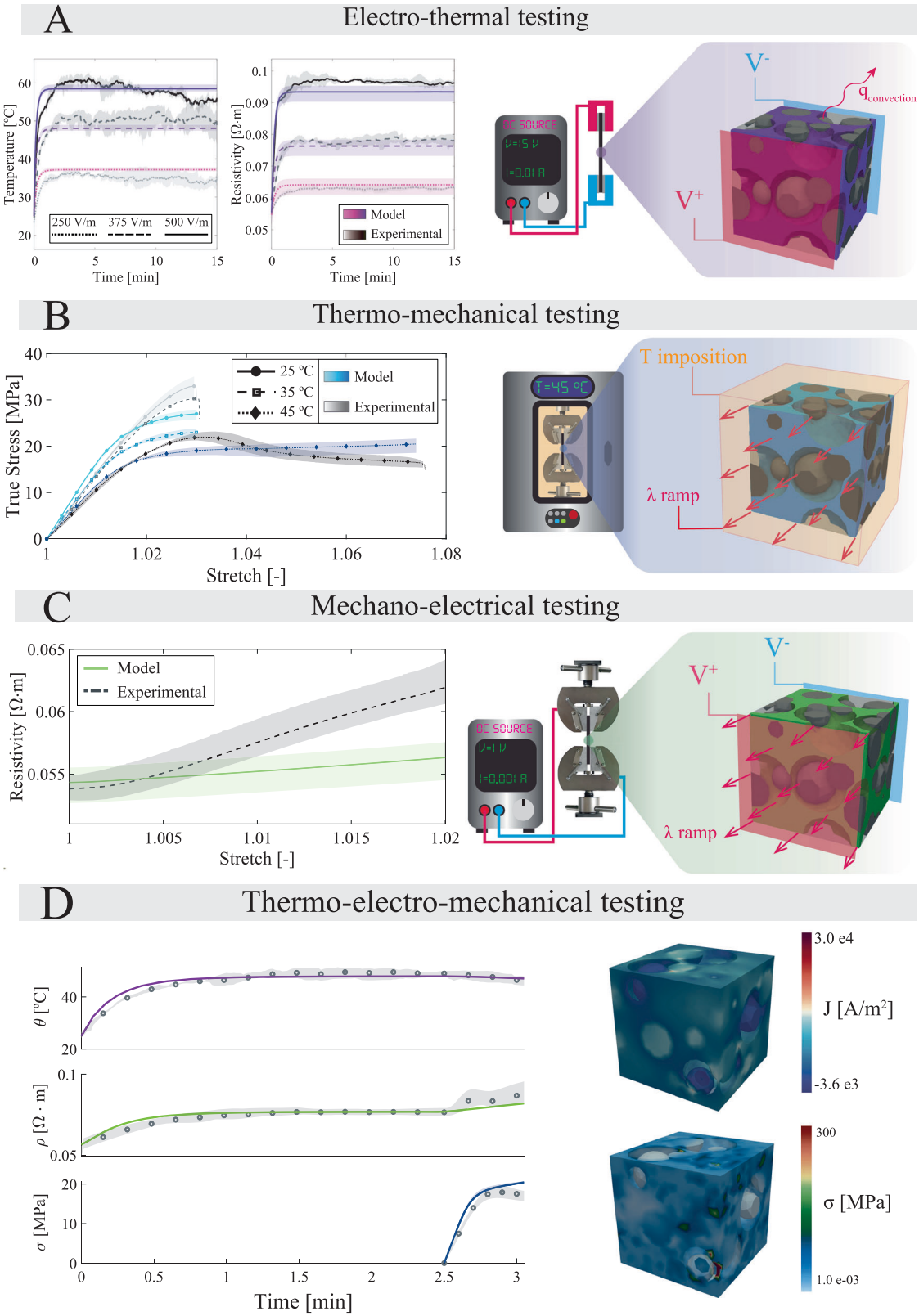

Fig. 3 Computational results from a full-field homogenisation framework explain the thermo-electro-mechanical response of conductive PLA from microstructural basis. A Electro-thermal simulations at three different applied electrical fields: 250 V m^{-1}, 375 V m^{-1}, and 500 V m^{-1}. Both temperature and resistivity are represented versus time. **B** Thermo-mechanical simulations for three temperatures: 25 °C, 35 °C, and 45 °C. True stress values are represented versus stretch. **C** Mechano-electrical simulations. Resistivity is represented versus stretch. **D** Thermo-electro-mechanical simulations representing the main studied variables over time. These simulations are divided in two steps: (i) an electric field is applied to the RVE, causing an increase in temperature due to Joule heating; (ii) after 2.5 min, a stretching ramp is applied while maintaining the electric field boundary conditions. Note that for **A**–**C** a scheme of the boundary conditions applied to the RVE is presented. The model predictions correspond to the mean of three RVEs simulations. All panels show both experimental and model data.

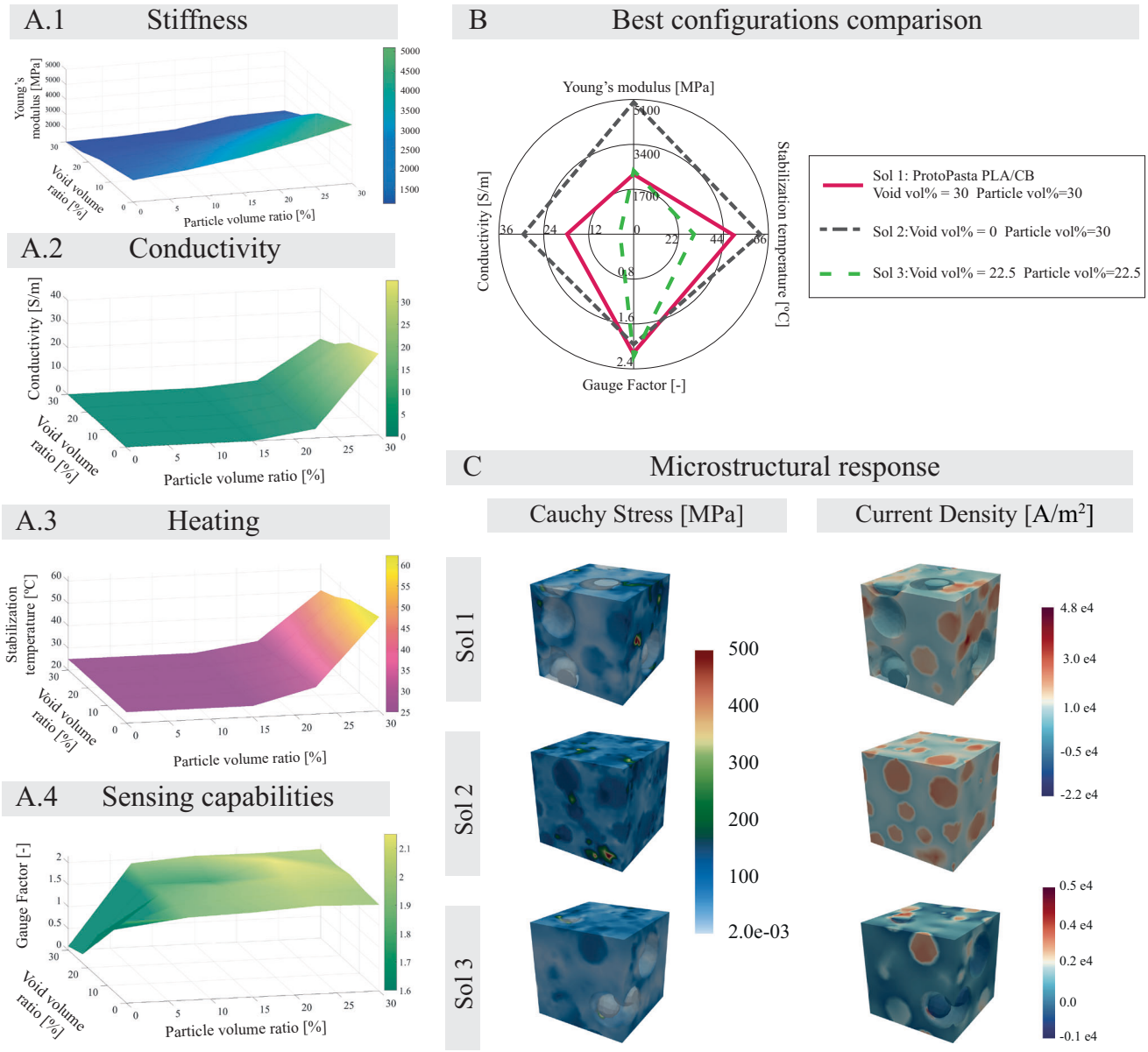

Fig. 4 The virtual testing framework enables to optimise the multi-physical capabilities of conductive PLA feedstock. A parametric sweep of particle and void volume ratios provides the main thermo-electro-mechanical properties of conductive PLA filaments: **A.1** Young's modulus; **A.2** apparent conductivity; **A.3** electro-thermal coupling, i.e., stabilisation temperature when applying a constant electric field of 375 V m^{-1}; **A.4** gauge factor. **B** Comparison of the best particles/voids volume ratio configurations to optimise stiffness, gauge factor and electro-thermal coupling. Three solutions are presented: Solution (1) with a particle volume ratio of 30% and void volume ratio of 30%, matching ProtoPasta conductive PLA; Solution (2) with a particle volume ratio of 30% and null void content; Solution (3) with a particle volume ratio of 22.5% and void volume ratio of 22.5%. **C** Microstructural response of the three proposed solutions in terms of: Left column) Cauchy stress at a macroscopic stretch of 1.02; Right column) current density when applying a constant electric field of 375 V m^{-1} (along the field direction).

sensors with complex geometries could be manufactured by using conductive PLA as feedstock. Overall, the experimental procedure provided in this work enables manufacturers to test their products under multifunctional loading conditions. In this regard, our approach could enhance the quality control of commercial filaments to ensure repeatability between spools, not only from the mechanical and electrical perspectives, but also from their interplays. Nevertheless, to account for the final operational stages of these materials, a different perspective would be needed. Dramatic changes in electrical conductivity and thermal responses within the composite occur under large mechanical deformations. To accurately describe such behaviours, the computational framework would need to incorporate a fracture model. To this end, cohesive elements may be used to consider particle-matrix debonding[54], or phase field fracture approaches may be used with a macroscopic scale modelling[55].

The presented computational framework offers a means for manufacturers to virtually optimise fabrication requirements to obtain desired properties in their final products, i.e., stiffer products, filaments with higher conductivities or with better sensing capabilities. To this end, parametric sweep studies of virtual tests can be performed considering void and particle contents, as well as the material properties of the phases (i.e., polymeric matrix and conductive particles), to achieve the optimal configuration for a given set of requirements. As a proof of concept, we performed a numerical analysis of the influence of

particles and void contents on the multifunctional performance of conductive PLA filaments. Taking altogether, these computational results show that there is not a unique solution for optimising material stiffness, conductivity, or heating and sensing capabilities, as the functional interplays between these properties are highly complex and affect one another, modulating the final composite performance. In Fig. 4, three different solutions were proposed, each considered as the best configuration for achieving the highest performance in a specific field, i.e., stiffness, conductivity, heating and sensing capabilities. For example, the configuration that shows the highest conductivity also presents the highest stabilisation temperature due to the high dependence of Joule heating on conductivity. This configuration is obtained for the RVEs with 30% particle content and null void content, which also presents the highest stiffness among all the configurations. It is worth noting that the ProtoPasta conductive filament corresponds to the configuration of 30% particle volume ratio and 30% void volume ratio, which exhibits one of the best sensing capabilities while maintaining a similar conductivity to the previous solution.

METHODS

Material and manufacture

Conductive PLA/CB filaments for FFF printers from ProtoPasta (WA, USA), with nominal and measured filament diameters of 1.75 mm and 1.72 mm, respectively, were used in this study as virgin filaments. The spool-filament samples were prepared with a length of 80 mm, allowing for a correct gripping area for the mechanical testing. To manufacture the extruded filaments, the same material was used as feedstock for a commercial FFF printer, specifically, the Prusa i3 MK3S+ (Prusa Research, Czech Republic). The extruder head was placed 20 cm away from the printing bed to ensure adequate cooling of the extruded filament. The composite was extruded at 230 °C through a hardened-steel nozzle with a diameter of 0.4 mm, resulting in a measured filament diameter of 0.385 mm.

Experimental procedure for electro-thermal tests

An adjustable DC power source was used in the experiments to supply a constant DC voltage (V_o) to the filaments. To ensure a consistent distance between electrodes (L) during test repetitions, as well as a correct electrical contact of the filaments, ad-hoc electrode grips were manufactured and attached to the universal testing machine. Those electrode grips consisted of 20 × 20 mm aluminium plates that ensured electrical contact with the gripped filaments. The distance between electrodes was set to 40 mm. Three voltages were considered: 10 V, 15 V and 20 V leading to the corresponding electrical fields of 250 V m^{-1}, 375 V m^{-1} and 500 V m^{-1}, respectively. The temperature of the samples was recorded by an infrared camera (FLUKE TiS75+, WA, USA). The resistivity of the material (ρ) was obtained by measuring the resistance of the samples (R_i) using a data-acquisition system (DATAQ DI-2008, OH, USA). As the data-acquisition system only measures voltage values, the material resistivity was calculated via voltage drop (V_{drop}) on an additional 1 Ω resistor (R_{ref}) connected in series. Then, the relation used to calculate the sample's resistivity from the measured voltage was the following:

$$\rho = \frac{R_i A}{L}; \quad R_i = \frac{R_{ref}(V_o - V_{drop})}{V_{drop}} \tag{1}$$

where A is the area of the sample's cross-section and V_o the applied voltage. This procedure was used for the virgin samples (Sections 'Introduction' and 'Results') as well as for the extruded-filament samples (Section 'Introduction').

Experimental procedure for thermo-mechanical tests

Uniaxial tensile tests (using the universal testing machine INSTRON 34TM-5, MA, USA) were performed on filament samples at a strain rate of 0.005 s^{-1} and using a climatic chamber (INSTRON 3119-605, MA, USA) to control the experiment temperature. A load cell of 5 kN was used, along with wedge action grips of 5 kN. These tests were performed at different testing temperatures of 25, 35, 45, 55 and 65 °C. These thermal conditions were controlled during the test by a type K thermocouple to limit fluctuations to ±1 °C. Prior to the tests, uniform temperature conditions were guaranteed by holding the samples for 15 min once the testing temperature was reached.

Experimental procedure for mechano-electrical tests

For this set of experiments, we performed uniaxial tensile tests (INSTRON 34TM-5, MA, USA) on filament samples at a strain rate of 0.00125 s^{-1}. Note that a slightly lower strain rate was used in these tests with respect to the thermo-mechanical tests to facilitate the synchronization of mechanical and electrical measurements. In addition, no significant rate dependences were observed between both testing rates. While applying the mechanical loading, the resistivity was measured using the procedure explained in Methods for electro-thermal tests. In this case, an additional in-series resistor of 465 Ω was used. This method was applied for both the commercial and extruded filament samples.

Experimental procedure for thermo-mechano-electrical tests

A combination of the experimental setups presented above, namely the electro-thermal and mechano-electrical tests, was used. These experiments consisted of two phases: (i) electro-thermal test in which a constant electric field of 375 V m^{-1} was applied to filament samples for two and a half minutes to ensure a correct temperature and resistivity stabilisation; and (ii) uniaxial tensile test at a strain rate of 0.00125 s^{-1} while maintaining the electric field. The resistivity was measured using an additional resistor of 1 Ω to obtain more accurate measures of the current flux through the filament that causes Joule heating.

Constitutive and computational framework of the full-field homogenised model

The microstructural computational framework aims to determine the homogenised macroscopic material behaviour by solving the electro-thermo-mechanical equilibrium at the microscopic level, considering both macroscopic loads and microstructural features[22,56]. This is achieved by generating a microscopic domain through the periodic repetition of a unit cell, also known as the Representative Volume Element (RVE), which represents the smallest sample of heterogeneity within the microstructure. For conductive PLA, the RVE includes a random arrangement of spherical particles and voids, which provides a realistic representation of its microstructure. This geometrical representation is enforced to be periodic and, in combination with periodic boundary conditions, assumes an idealized perfect infinite arrangement of random particles and voids. Then, the full-field coupled electro-thermo-mechanical problem is posed and solved in a periodic fixed domain defined in the reference configuration where three phases are considered: the matrix, the voids, and the conductive particles. Therefore, the problem field variables to be solved are the displacement field, $\mathbf{u}$, the electric potential field, ϕ, and the temperature field, θ.

Within the RVE, the mechanical response of the different phases is assumed to behave as an elastic-viscoplastic solid. The proposed rheological model consists of two parallel branches[57]. The total first Piola-Kirchhff stress ($\mathbf{P}$) is decomposed into the stress $\mathbf{P}_A$ due to the intermolecular resistance (branch A), which accounts for a plastic flow; and the stress $\mathbf{P}_B$ due to the network resistance (branch B), which exhibits a purely hyperelastic behaviour. The intermolecular resistance is defined by a compressible Neo-

Hookean model as

$$\mathbf{P}_{\mathrm{A}}(\mathbf{F},\mathbf{F}^{\mathrm{p}},\theta)=[\mu(\theta)(\mathbf{B}^{\mathrm{e}}-\mathbf{I})+\lambda(\theta)ln(J_F^{\mathrm{e}})\mathbf{I}]\cdot(\mathbf{F}^{-1})^{T} \tag{2}$$

where $\mu(\theta)$ and $\lambda(\theta)$ are the temperature-dependent Lamé constants, $\mathbf{B}^{\mathrm{e}}=\mathbf{F}^{\mathrm{e}}(\mathbf{F}^{\mathrm{e}})^{T}$ and $\mathbf{J}_F^{\mathrm{e}}=\det(\mathbf{F}^{\mathrm{e}})$. Note that the elastic constants are defined as temperature-dependent and follow a linear relation with the temperature (see Supplementary Methods). The plastic deformation of this branch follows the multiplicative decomposition of the deformation gradient into elastic, $\mathbf{F}^{\mathrm{e}}$, and plastic, $\mathbf{F}^{\mathrm{p}}$, components; $\mathbf{F}=\mathbf{F}^{\mathrm{e}}\mathbf{F}^{\mathrm{p}}$. The plastic behaviour is dictated by the isotropic yield surface

$$f=\overline{\sigma}_{\mathrm{VM}}-\sigma_{\mathrm{Y}}(\theta)-k(\theta) \tag{3}$$

where $\overline{\sigma}_{\mathrm{VM}}$ is the Von Mises equivalent stress and σ_{Y} and k are the yield stress and the isotropic hardening (Voce law), respectively, which are considered temperature-dependent (see Supplementary Methods). The plastic flow reads

$$\dot{\overline{\varepsilon}}^{\mathrm{p}}=\begin{cases}\dot{\varepsilon}_{\mathrm{o}}\left(\exp\left[\frac{1}{C}\left(\frac{\overline{\sigma}_{\mathrm{A}}}{\sigma_{\mathrm{Y}}+k}\right)-1\right]-1\right) & f>0\\ 0 & f<=0\end{cases} \tag{4}$$

where $\dot{\varepsilon}_{\mathrm{o}}$ is the reference strain rate and C is the strain-rate sensitivity parameter[57]. The plastic flow direction follows the deviatoric part of the Cauchy stress $\mathbf{N}=\sqrt{3/2}\,\boldsymbol{\sigma}_{\mathrm{A}}^{\mathrm{dev}}/\|\boldsymbol{\sigma}_{\mathrm{A}}^{\mathrm{dev}}\|$, defining the rate of plastic deformation gradient as $\dot{\mathbf{F}}^{\mathrm{p}}=(\mathbf{F}^{\mathrm{e}})^{-1}\cdot\dot{\overline{\varepsilon}}^{\mathrm{p}}\mathbf{N}\cdot\mathbf{F}$. The network resistance (branch B) is defined with an eight-chain elastic model by

$$\mathbf{P}_{\mathrm{B}}(\mathbf{F},\theta)=\left[\frac{C_{\mathrm{R}}(\theta)}{3}\frac{\overline{\lambda}_{\mathrm{L}}}{\overline{\lambda}}\mathcal{L}^{-1}\left(\frac{\overline{\lambda}}{\overline{\lambda}_{\mathrm{L}}}\right)(\mathbf{B}_{\mathrm{B}}^{*}-\overline{\lambda}^{2}\mathbf{I})+Kln(J_F)\mathbf{I}\right]\cdot(\mathbf{F}^{-1})^{T} \tag{5}$$

where $\mathbf{B}^{*}=\mathbf{F}^{*}(\mathbf{F}^{*})^{T}$, with $\mathbf{F}^{*}=J_F^{-\frac{1}{3}}\mathbf{F}$, $\overline{\lambda}=\sqrt{\frac{1}{3}tr(\mathbf{B}^{*})}$ is the effective distortional stretch, $\overline{\lambda_{\mathrm{L}}}$ is the locking stretch[58], $\mathbf{I}$ is the identity second order tensor, $J_F=\det(\mathbf{F})$, K is the bulk modulus and $C_{\mathrm{R}}(\theta)$ is the temperature-dependent stiffness of branch B. $\mathcal{L}^{-1}$ represents the inverse Langevin function, approximated as $\mathcal{L}^{-1}(x)=\frac{3x}{1-x^{3}}$. The field equation for the mechanical equilibrium is set as a linear momentum balance under the absence of body forces, and defined in the reference configuration as

$$\nabla_{\mathbf{X}}\cdot\mathbf{P}=0 \tag{6}$$

where $\nabla_{\mathbf{X}}$ is the gradient operator with respect to the reference configuration.

Regarding the electrostatic problem within the RVE, all phases provide a linear relation between electric current density ($\mathbf{j}$) and electric field, which can be expressed in the current configuration as

$$\mathbf{j}=\sigma\mathbf{e} \tag{7}$$

where $\mathbf{e}(\mathbf{x})=-(\mathbf{F}^{-1})^{T}\cdot\nabla_{\mathbf{X}}\phi(\mathbf{X})$ is the electric field in the current configuration ($\phi(\mathbf{X})$ is the electric potential), and σ is the electrical conductivity. Thus, the electric current density as a function of the electric field $\mathbf{E}(\mathbf{X})$ in the reference configuration reads

$$\mathbf{J}=J_F\mathbf{F}^{-1}\mathbf{j}=\sigma(\theta)J_F\mathbf{F}^{-1}\cdot(\mathbf{F}^{-1})^{T}\cdot\mathbf{E}. \tag{8}$$

The governing equations for the electrostatic problem correspond to the Maxwell's equations along with the continuity equation:

$$\nabla_{\mathbf{X}}\cdot\mathbf{D}=Q;\quad\nabla_{\mathbf{X}}\times\mathbf{E}=0;\quad\nabla_{\mathbf{X}}\cdot\mathbf{J}=0 \tag{9}$$

with Q being the charge accumulated within the body. Note that the second equation is automatically accomplished by the definition of the electric field as a gradient of a scalar potential. To account for the current flow between near particles separated by a thin film of polymeric matrix, the matrix conductivity was modified depending on the average distance between particles within the RVE[59] (see Supplementary information for more details):

$$\sigma_{\mathrm{o}}^{\mathrm{m}}=\left(\frac{h}{e^{2}\sqrt{2m\lambda}}\exp\left(\frac{4\pi\overline{d}}{h}\sqrt{2m\lambda}\right)\right)^{-1}, \tag{10}$$

with $\sigma_{\mathrm{o}}^{\mathrm{m}}$ as the matrix conductivity in the tunneling effect zone at reference temperature, h as the Planck constant, e as the electron charge, m as the electron mass, λ as the barrier height and $\overline{d}$ as the mean distance between particle's aggreagates within the RVE.

From the second law of thermodynamics, the thermal governing equation as transient heat balance is derived as

$$\varrho\dot{\theta}-\nabla_{\mathbf{X}}(\kappa J_F\mathbf{F}^{-1}\cdot(\mathbf{F}^{-1})^{T}\cdot\nabla_{\mathbf{X}}\theta)-\mathcal{R}=0 \tag{11}$$

where ϱ is the volumetric heat capacity (density in the reference configuration multiplied by heat capacity), κ is the thermal conductivity and $\mathcal{R}$ is the volumetric heat resource, caused by Joule effect. The heat source can be written as:

$$\mathcal{R}=\mathbf{J}\cdot\mathbf{E}. \tag{12}$$

To obtain the macroscopic effective behaviour and by applying homogenisation concepts, the total displacement field, $\mathbf{u}(\mathbf{X})$, can be decomposed into a macroscopic variation and a fluctuating displacement field $\tilde{u}(\mathbf{X})$ as

$$\mathbf{u}(\mathbf{X})=(\overline{\mathbf{F}}-\mathbf{I})\cdot\mathbf{X}+\tilde{\mathbf{u}}(\mathbf{X}). \tag{13}$$

Similarly, the electric potential field ϕ can be decomposed into a macroscopic contribution and a fluctuating electric potential field $\tilde{\phi}$ as

$$\phi=-\overline{\mathbf{E}}\cdot\mathbf{X}+\tilde{\phi}. \tag{14}$$

While the temperature field θ can be decomposed into a Lagrange multiplier contribution λ_{th}, that accounts for the convective BCs (see Supplementary Methods for more details), and a fluctuating temperature $\tilde{\theta}$ as

$$\theta=\lambda_{th}+\tilde{\theta}. \tag{15}$$

In the full-field homogenisation problem, the fluctuating variables are implicitly solved by the governing field equations, resulting in the macroscopic behaviour as a function of the macroscopic test inputs, introduced as BCs (see Supplementary Methods for more details). The Jacobian submatrices of the problem were symbolically derived from the residuals. The followed computational approach, consisting in a fully-coupled scheme, was solved in an implicit monolithic manner.

Computational details for the generation of microstructural RVEs

Periodic RVEs with three phases were obtained by modelling the void phase and conductive particle phases as sets of spheres. The position of the different spheres was controlled by a Monte Carlo algorithm, placing them in a random fashion while ensuring different geometrical restrictions: (i) Void spheres can overlap, allowing to form complex void geometries similar to those observed in SEM images; (ii) Particles sets were formed by using two different sphere radius, to emulate particle clusters and individual particles; (iii) The particles cannot overlap. Additional RVEs configurations were used: (i) RVEs formed by polymeric matrix and micro-voids; (ii) RVEs formed by polymeric matrix and particles; (iii) RVEs formed only by polymeric matrix. The same Monte Carlo algorithm and geometrical restrictions were considered to create two-phases RVEs. Every geometry was meshed by using tetrahedral elements, using the free-software GMSH. The SEM images allowed for identifying the main geometrical features of the microstructure such as the dispersion of particles, formation of

aggregates and distribution of voids. This information was used to generate the FE meshes of the RVEs.

DATA AVAILABILITY

All data generated and analysed during this study is available from the corresponding author upon reasonable request.

CODE AVAILABILITY

The code generated during this study is available from the corresponding author upon reasonable request.

Received: 8 May 2023; Accepted: 19 July 2023;
Published online: 31 July 2023

REFERENCES

1. Tan, J. C. & Low, H. Y. Multi-materials fused filament printing with embedded highly conductive suspended structures for compressive sensing. *Addit. Manuf.* **36**, 101551 (2020).
2. Kim, S. et al. Wearable, ultrawide-range, and bending-insensitive pressure sensor based on carbon nanotube network-coated porous elastomer sponges for human interface and healthcare devices. *ACS Appl. Mater. Interfaces* **11**, 2022 (2019).
3. Lopez-Donaire, M. L. et al. Computationally guided DIW technology to enable robust printing of inks with evolving rheological properties. *Adv. Mater. Technol.* **8**, 2201707 (2023).
4. Zhong, Y., An, R., Ma, H. & Wang, C. Low-temperature-solderable intermetallic nanoparticles for 3d printable flexible electronics. *Acta Mater.* **162**, 163–175 (2019).
5. Rahaman, M. et al. Predicting percolation threshold value of EMI SE for conducting polymer composite systems through different sigmoidal models. *J. Electron. Mater* **51**, 1788–1803 (2022).
6. Mamunya, Y. P., Davydenko, V. V., Pissis, P. & Lebedev, E. V. Electrical and thermal conductivity of polymers filled with metal powders. *Eur. Polym. J.* **38**, 1887–1897 (2002).
7. Psarras, G. C. Hopping conductivity in polymer matrix-metal particles composites. *Compos. A Appl. Sci.* **37**, 1545–1553 (2006).
8. Lei, Z. et al. Novel electrically conductive composite filaments based on ag/saturated polyester/polyvinyl butyral for 3d-printing circuits. *Compos. Sci. Technol.* **180**, 44–50 (2019).
9. Borghetti, M., Serpelloni, M. & Sardini, E. Printed strain gauge on 3d and low-melting point plastic surface by aerosol jet printing and photonic curing. *Sensors* **19**, 4220 (2019).
10. Dong, K., Panahi-Sarmad, M., Cui, Z., Huang, X. & Xiao, X. Electro-induced shape memory effect of 4d printed auxetic composite using pla/tpu/cnt filament embedded synergistically with continuous carbon fiber: a theoretical and experimental analysis. *Compos. B Eng.* **220**, 108994 (2021).
11. Dorigato, A., Moretti, V., Dul, S., Unterberger, S. H. & Pegoretti, A. Electrically conductive nanocomposites for fused deposition modelling. *Synth. Met.* **226**, 7–14 (2017).
12. Lee, J., Emon, M. O. F., Vatani, M. & Choi, J.-W. Effect of degree of crosslinking and polymerization of 3d printable polymer/ionic liquid composites on performance of stretchable piezoresistive sensors. *Smart Mater. Struct.* **26**, 035043 (2017).
13. Kaynan, O., Yıldız, A., Bozkurt, Y. E., Yenigun, E. O. & Cebeci, H. Electrically conductive high-performance thermoplastic filaments for fused filament fabrication. *Compos. Struct.* **237**, 111930 (2020).
14. Lei, L., Qiu, J. & Sakai, E. Preparing conductive poly(lactic acid) (pla) with poly(-methyl methacrylate) (pmma) functionalized graphene (pfg) by admicellar polymerization. *Chem. Eng. J.* **209**, 20–27 (2012).
15. Qian, Y., Li, C., Qi, Y. & Zhong, J. 3d printing of graphene oxide composites with well controlled alignment. *Carbon* **171**, 777–784 (2021).
16. Gnanasekaran, K. et al. 3d printing of cnt- and graphene-based conductive polymer nanocomposites by fused deposition modeling. *Appl. Mater. Today* **9**, 21–28 (2017).
17. Wang, W. & Jayatissa, A. H. Computational and experimental study of electrical conductivity of graphene/poly(methyl methacrylate) nanocomposite using monte carlo method and percolation theory. *Synth. Met.* **204**, 141–147 (2015).
18. Leigh, S. J., Bradley, R. J., Purssell, C. P., Billson, D. R. & Hutchins, D. A. A simple, low-cost conductive composite material for 3d printing of electronic sensors. *PLoS One* **7**, e49365 (2012).
19. Lazarus, N. & Bedair, S. S. Creating 3d printed sensor systems with conductive composites. *Smart Mater. Struct.* **30**, 015020 (2021).
20. Wu, T. & Chen, B. Facile fabrication of porous conductive thermoplastic polyurethane nanocomposite films via solution casting open. *Sci. Rep.* **7**, 17470 (2017).
21. Crespo-Miguel, J. et al. Thermo-electro-mechanical aging and degradation of conductive 3d printed pla/cb composite. *Compos. Struct.* **316**, 116992 (2023).
22. Kanan, A., Vasilev, A., Breitkopf, C. & Kaliske, M. Thermo-electro-mechanical simulation of electro-active composites. *Materials* **15**, 783 (2022).
23. Nordin, N. M., Buys, Y. F., Anuar, H., Ani, M. H. & Pang, M. M. Development of conductive polymer composites from pla/tpu blends filled with graphene nanoplatelets. *Mater. Today Proc.* **17**, 500–507 (2019).
24. Postiglione, G., Natale, G., Griffini, G., Levi, M. & Turri, S. Conductive 3d microstructures by direct 3d printing of polymer/carbon nanotube nanocomposites via liquid deposition modeling. *Compos. A Appl. Sci. Manuf.* **76**, 110–114 (2015).
25. Kim, H. & Lee, S. Characterization of electrical heating of graphene/pla honeycomb structure composite manufactured by cfdm 3d printer. *Fash. Text* **7**, 8 (2020).
26. Flowers, P. F., Reyes, C., Ye, S., Kim, M. J. & Wiley, B. J. 3d printing electronic components and circuits with conductive thermoplastic filament. *Addit. Manuf.* **18**, 156–163 (2017).
27. Nankali, M., Nouri, N. M., Malek, N. G. & Amjadi, M. Dynamic thermoelectromechanical characterization of carbon nanotube nanocomposite strain sensors. *Sens. Actuator A Phys.* **332**, 113122 (2021).
28. Fu, F., Wang, J., Zeng, H. & Yu, J. Functional conductive hydrogels for bioelectronics. *ACS Mater. Lett.* **2**, 1287–1301 (2020).
29. Zhang, Y.-Z. et al. Mxenes stretch hydrogel sensor performance to new limits. *Sci. Adv.* **4**, eaat0098 (2018).
30. Li, L. et al. All inkjet-printed amperometric multiplexed biosensors based on nanostructured conductive hydrogel electrodes. *Nano Lett.* **18**, 3322–3327 (2018).
31. Han, L. et al. Mussel-inspired adhesive and conductive hydrogel with long-lasting moisture and extreme temperature tolerance. *Adv. Funct. Mater.* **28**, 1704195 (2018).
32. Yang, Y. & Jiao, P. Nanomaterials and nanotechnology for biomedical soft robots. *Mater. Today Adv.* **17**, 100338 (2023).
33. Hsiao, L. Y. et al. Carbon nanotube-integrated conductive hydrogels as multifunctional robotic skin. *Carbon* **161**, 784–793 (2020).
34. Roels, E. et al. Self-healing sensorized soft robots. *Mater. Today Electronics* **1**, 100003 (2022).
35. Namitha, L. K. & Sebastian, M. T. High permittivity ceramics loaded silicone elastomer composites for flexible electronics applications. *Ceram. Int.* **43**, 2994–3003 (2017).
36. Yoo, J. I. et al. Thermal shape morphing of membrane-type electronics based on plastic-elastomer frameworks for 3d electronics with various gaussian curvatures. *Mater. Des.* **227**, 111811 (2023).
37. Liu, X. et al. Biomimetic integration of tough polymer elastomer with conductive hydrogel for highly stretchable, flexible electronic. *Nano Energy* **92**, 106735 (2022).
38. Li, Y. et al. Biodegradable thermal imaging-tracked ultralong nanowire-reinforced conductive nanocomposites elastomers with intrinsical efficient antibacterial and anticancer activity for enhanced biomedical application potential. *Biomater.* **201**, 68–76 (2019).
39. Wu, T. et al. The orientation and inhomogeneous distribution of carbon nanofibers and distinctive internal structure in polymer composites induced by 3d-printing enabling electromagnetic shielding regulation. *J. Colloid Interface Sci.* **638**, 392–402 (2023).
40. Garzon-Hernandez, S., Arias, A. & Garcia-Gonzalez, D. A continuum constitutive model for fdm 3d printed thermoplastics. *Compos. B Eng.* **201**, 108373 (2020).
41. Moyo, M., Kanny, K. & Mohan, T. P. Thermo-mechanical response of kenaf/pla biocomposites to clay nanoparticles infusion. *Mater. Today Proc.* **38**, 609–613 (2021).
42. Tirado-Garcia, I. et al. Conductive 3d printed pla composites: On the interplay of mechanical, electrical and thermal behaviours. *Compos. Struct.* **265**, 113744 (2021).
43. Ghosh, K., Ng, S., Iffelsberger, C. & Pumera, M. 2d mos2/carbon/polylactic acid filament for 3d printing: Photo and electrochemical energy conversion and storage. *Appl. Mater. Today* **26**, 101301 (2022).
44. Rocha, R. G. et al. Production of 3d-printed disposable electrochemical sensors for glucose detection using a conductive filament modified with nickel microparticles. *Anal. Chim. Acta* **1132**, 1–9 (2020).
45. Stefano, J. S. et al. New conductive filament ready-to-use for 3d-printing electrochemical (bio)sensors: Towards the detection of sars-cov-2. *Anal. Chim. Acta* **1191**, 339372 (2022).
46. Kwok, S. W. et al. Electrically conductive filament for 3d-printed circuits and sensors. *Appl. Mater. Today* **9**, 167–175 (2017).

47. Stopforth, R. Conductive polylactic acid filaments for 3d printed sensors: Experimental electrical and thermal characterization. *Sci. Afr.* **14**, e01040 (2021).
48. Roumy, L., Touchard, F., Marchand, D., Hoang, T. Q. T. & Martinez-Hergueta, F. Durability of joule effect of 3d printed carbon black/polylactic acid: electrical cyclic tests and analytical modelling. *Int. J. Fatigue* **173**, 107677 (2023).
49. Niendorf, K. & Raeymaekers, B. Combining ultrasound directed self-assembly and stereolithography to fabricate engineered polymer matrix composite materials with anisotropic electrical conductivity. *Compos. B Eng.* **223**, 109096 (2021).
50. Ba, M., Zhang, Z. & Qi, Y. The dispersion tolerance of micro/nano particle in polydimethylsiloxane and its influence on the properties of fouling release coatings based on polydimethylsiloxane. *Coatings* **7**, 107 (2017).
51. Gbaguidi, A., Namilae, S. & Kim, D. Stochastic percolation model for the effect of nanotube agglomeration on the conductivity and piezoresistivity of hybrid nanocomposites. *Comput. Mater. Sci.* **166**, 9–19 (2019).
52. Zhang, P. & Pan, T. Exact analytical theory for inverse tunneling of free vacuum electrons into a solid. *AIP Adv.* **7**, 065307 (2017).
53. Rong, Z., Yuezhen, B., Ru, C. & Masaru, M. Evaluation by tunneling effect for the temperature-dependent electric conductivity of polymer-carbon fiber composites with visco-elastic properties. *Polym. J.* **45**, 1120–1134 (2013).
54. Spring, D. W. & Paulino, G. H. Computational homogenization of the debonding of particle reinforced composites: the role of interphases in interfaces. *Comput. Mater. Sci.* **109**, 209–224 (2015).
55. Moreno-Mateos, M. A., Hossain, M., Steinmann, P. & Garcia-Gonzalez, D. Hard magnetics in ultra-soft magnetorheological elastomers enhance fracture toughness and delay crack propagation. *J. Mech. Phys. Solids* **173**, 105232 (2023).
56. Otto, M., Schutzeichel, H., Kletschkowski, T. & Monner, H. P. Microscale thermal modelling of multifunctional composite materials made from polymer electrolyte coated carbon fibres including homogenization and model reduction strategies. *Appl. Mech.* **2**, 739–765 (2021).
57. Polanco-Loria, M., Clausen, A. H., Berstad, T. & Hopperstad, O. S. Constitutive model for thermoplastics with structural applications. *Int. J. Impact Eng.* **37**, 1207–1219 (2010).
58. Bergström, J. 5 - elasticity/hyperelasticity. In *Mechanics of Solid Polymers* (ed Bergström, J.) 209–307 (William Andrew Publishing, 2015).
59. Haghgoo, M., Ansari, R. & Hassanzadeh-Aghdam, M. K. The effect of nanoparticle conglomeration on the overall conductivity of nanocomposites. *Int. J. Eng. Sci.* **157**, 103392 (2020).

ACKNOWLEDGEMENTS

The authors acknowledge support from the European Research Council (ERC) under the European Union's Horizon 2020 research and innovation programme (grant agreement No.947723, project: 4D-BIOMAP) and from the Ministerio de Ciencia, Innovacion y Universidades under the Plan Nacional 2018 (RTI2018-094318-B-I00) and the Plan Nacional 2021 (PID2021-123294OB-I00). J.C.M. acknowledges support from the Ministerio de Ciencia, Innovacion y Universidades, Spain (PRE2019-089276). S.L. was funded by the Marie Skłodowska-Curie Individual Fellowship 101031287 under the EU Horizon 2020 Framework Programme for Research and Innovation.

AUTHOR CONTRIBUTIONS

All authors conceived the research. J.C.M. performed the experiments. J.C.M., S.L. and D.G.G. implemented the computational model and wrote the original manuscript. All authors conducted the formal analysis, discussion and revised the paper.

COMPETING INTERESTS

The authors declare no competing interests.

ADDITIONAL INFORMATION

Supplementary information The online version contains supplementary material available at https://doi.org/10.1038/s41524-023-01091-8.

Correspondence and requests for materials should be addressed to Daniel Garcia-Gonzalez.

Reprints and permission information is available at http://www.nature.com/reprints

Publisher's note Springer Nature remains neutral with regard to jurisdictional claims in published maps and institutional affiliations.